Reviews of Modern Plasma Physics (2025) 9:27
https://doi.org/10.1007/s41614-025-00199-2

SPECIAL TOPICS

State of the art of gyrokinetic and hybrid MHD-kinetic codes through non-linear benchmarking to study reactor relevant burning plasmas

Gregorio Vlad · Xin Wang · Francesco Vannini · Hinrich Lütjens · Sergio Briguglio · Nakia Carlevaro, et al. ***[full author details at the end of the article]***

Received: 2 January 2025 / Accepted: 30 June 2025

Abstract

After a brief introduction on present day simulation and modeling of burning plasmas in magnetically confined devices, the results of a non-linear benchmark are presented, undertaken among several state-of-the-art codes available to study the self-consistent interaction of an Energetic Particle (EP) population with shear Alfvén waves: HYMAGYC, MEGA, ORB5 and XTOR-K. The first two codes, HYMAGYC and MEGA, are hybrid codes: HYMAGYC is a MHD-Gyrokinetic code (the bulk plasma is represented by MHD equations, while the EP species is treated using the gyrokinetic formalism), while MEGA is an MHD-Drift-Kinetic code (the bulk plasma is represented by MHD equations, while the EP species is treated using the drift-kinetic formalism, with the possibility of an ad-hoc gyroaveraging); ORB5 is a global electromagnetic gyrokinetic code (both bulk and EP species are treated using the gyrokinetic formalism); XTOR-K is a non-linear kinetic-MHD code (the bulk plasma is described by a set of non-linear resistive two-fluid MHD equations, extended to include kinetic effects of multiple ion species with a fully kinetic PIC module). The equilibrium of the so-called NLED-AUG reference case, in its version with peaked off-axis EP density profile, has been used, while considering a $|n| = 1$ perturbation. This non-linear benchmark is the natural continuation of the linear benchmark already considered in the recent past, and represent a first-ever code comparison in the deep non-linear stage. In the present study fluid non-linearities are omitted, and the focus will be on comparing wave-particle interactions effects across codes. Characteristics of the non-linear saturation of the mode, self-consistent modification to the EP density profile and other features are compared among the considered codes. This brief review presents the state of the art of gyrokinetic and hybrid MHD-kinetic codes emerging as tools for studying reactor-relevant burning plasmas in realistic conditions.

Keywords Hybrid MHD-gyrokinetic simulation · Non-linear simulation · Gyrokinetic simulation · Kinetic-MHD simulation · Energetic particles · Alfvénic modes · Numerical simulations · Particle-in-cell method · Ideal and resistive MHD modes

1 Introduction

The research on controlled thermonuclear fusion plasmas is currently experiencing a particularly significant moment in its development: the latest generation of experimental devices have obtained a significative production of energy generated in thermonuclear reactions: the latest deuterium-tritium (DT) campaign in JET (Hobirk 2023), the Joint European Torus at Culham, UK (the largest magnetically confined device in the world) obtained the largest amount of energy ever achieved in a fusion experiment, while the NIF (Abu-Shawareb 2024) (the National Ignition Facility, California, US, the largest laser-driven device for inertial confinement) obtained the even more extraordinary result of generating a total fusion energy exceeding the laser energy input (target gain $G_{\text{target}} > 1$). The extensive study of such conditions will be the goal of next-generation devices, which should be able to operate in regimes well beyond the breakeven. We will deal, in the present review, only with magnetic confinement devices (e.g., tokamaks) for controlled thermonuclear fusion, and, thus, neglect inertial fusion research. These plasmas, usually referred as "burning plasmas", are in such a condition that the fusion energy released by the fusion products themselves is sufficient to self-sustain the necessary plasma temperature.

Next generation fusion devices include ITER (https://www.iter.org/) and CFETR (Special Issue 2022), and later on, DEMO (Hong 2022; Donné 2018; Federici 2018) class devices; but also medium-size machines which should address specific burning plasma issues in the near future (as, e.g., JT-60SA (https://www.jt60sa.org/wp/), BEST (Conroy 2024), and DTT (Martone et al. 2019)), not to mention the rapidly increasing number of devices proposed by private enterprises that have entered impetuously the international landscape in recent years. To design the next generation devices, and to prepare adequately the regimes of operation in such experiments, theoretical research and first principles-based numerical simulations and modeling activity are necessary, in particular because the burning plasma regime is still largely unexplored. Indeed, reactor-relevant plasmas are characterized by the presence of a large amount of highly energetic (3.5MeV) alpha particles, generated in nuclear fusion reactions, and which are envisaged to strongly interact, non-linearly, with the bulk plasma (DT) components.

As it is well known (ITER Physics Expert Group 1999), fusion alphas, characterized by thermal velocity of the order of Alfvén velocity, are expected to resonantly interact with Alfvén modes (as, e.g., Toroidal Alfvén Eigenmodes, TAEs); their mutual interaction could drive these globally extended Alfvénic modes unstable and, in turn, non-linearly induce radial transport of the energetic particles (EPs) themselves before their thermalization. As a consequence, enhanced EP losses could happen, with possible damage of the device itself, and/

or reduction of fusion performances, because of the decreasing of the EP density in the central part (close to the magnetic axis) of the plasma discharge. Several reviews have been published in the past decades regarding the shear Alfvén wave dynamics and their mutual interaction with energetic particles in reactor-relevant plasmas. We provide a short list here to assist readers: the "Chapter 5: Physics of energetic ions" in the ITER Physics Basis volumes from 1999 (ITER Physics Expert Group 1999) and 2007 (Fasoli et al. 2007), two introductory works on the dynamics of Alfvén waves and energetic particle interactions in toroidal plasmas (Vlad et al. 1999; Todo 2019), a specific review focusing on energetic ions in ITER plasmas (Pinches et al. 2015), a comprehensive review covering both linear and non-linear physics within a single unified theoretical framework, the so-called general fishbone-like dispersion relation (GFLDR) (Chen and Zonca 2016), and a specialized review on the gyrokinetic theory of TAE saturation via non-linear wave-wave coupling (Qiu et al. 2023).

Energetic particles will also act as mediators (Chen and Zonca 2016) of widely different scale couplings, from micro-scales (the characteristic length of the bulk plasma transport, $L \sim \rho_\mathrm{i}$, being ρ_i the bulk ion Larmor radius) to macro-scales (the characteristic length of magnetohydrodynamics (MHD) instabilities, $L \sim a$, being a the minor radius of the plasma torus) through meso-scales (with intermediate characteristic scale, $L \sim \rho_\mathrm{h}$, being ρ_h the energetic particle (alphas) Larmor radius).

A large effort has been undertaken in the recent past to study the turbulence and the anomalous thermal and particle diffusion in presence of energetic ions (both generated by auxiliary power sources (ICRH, NBI) and by fusion reactions) in the present day experiments, where evidence of turbulence reduction and/or improvements of confinement has been observed (see, e.g., Ref. Citrin and Mantica (2023) for an overview of this issue). The stabilizing effect of energetic particles on microturbulence and the ensuing confinement enhancement has been also highlighted in energetic particle dominant low-density discharges in KSTAR (Han 2022). The evolution characteristics of energetic particle modes (EPMs) in such a discharge condition have also been reported (JHang 2023). Due to the strong EP contribution to plasma beta (the ratio between plasma pressure and magnetic pressure) in those discharges, the subsequent analyses attribute the fast ion dilution effects as the dominant mechanism for the turbulence stabilization (Hahm 2023; Kim 2023).

A kinetic description of both thermal plasma components and energetic particles is required to describe properly the system, and the gyrokinetic formalism, which orders out the gyration motion of charged particles around the magnetic field lines, has been shown to be one of the most promising approaches. Both local (e.g., GENE (Jenko et al. 2000) in the local, flux-tube limit) and global (e.g., GTC (Liu et al. 2022), GENE (Di Siena et al. 2022) (run as a global code), GYRO (Waltz and Bass 2014) (here, transport solver simulations are coupled to the local GYRO model), GKNET (Ishizawa et al. 2021) and ORB5 (Biancalani 2021; Vannini 2022; Wang 2023) full plasma simulations) gyrokinetic codes have been used. Numerical evidence has been shown that global (full plasma) simulations, and electrostatic as well as electromagnetic perturbations, are required to properly describe the occurrence of meso-scale structures (zonal flow, zonal structures) which can, in turn, regulate the bulk turbulence (Di Siena 2023).

On the other hand, to better understand the mutual interaction between energetic particles and global, macro-scale modes (as, e.g., MHD modes), and also to reduce the highly demanding numerical resources required by global gyrokinetic simulations, reduced models have been proposed. The most promising one is the hybrid MHD-(gyro)kinetic model (Park 1992), in which the bulk plasma is described using fluid (MHD) equations, while the energetic particles are described by gyrokinetic (or full orbit) formalism, the two systems being coupled together by a proper coupling term in the fluid momentum equation (either the divergence of the EP pressure tensor term or the EP current and charge densities). Note that, to describe properly the mutual interaction between EPs and Alfvén waves, fluid equations and EPs must be considered self-consistently, i.e., a non-perturbative approach is also required. Examples of such types of hybrid MHD-gyrokinetic codes are M3D-K (Fu et al. 2006), HMGC (Briguglio et al. 1995, 1998), MEGA (Todo 2006), HYMAGYC (Fogaccia et al. 2016). Recent applications of those codes to the non-linear dynamics of EP-driven Alfvénic modes can be found, e.g.: for M3D-K, in Ref. Zhang (2024) (where simulations of beam-driven instabilities in KSTAR discharges are studied) and Ref. Duan et al. (2023) (where the interaction between EP beta-induced Alfvén eigenmode (BAE) and a tearing mode is studied with reference to a HL-2A experiment); for HMGC, in Ref. Wang et al. (2019) (with the study of the non-linear dynamics of shear Alfvén fluctuations in Divertor Tokamak Test (DTT) facility plasmas), in Ref. Wang et al. (2020, 2024) (with studies of the interaction between Reversed Shear Alfvén eigenmodes (RSAEs) and EPs), and in Ref. Wang (2022) (where a thorough analysis of the non-linear dynamics of a chirping frequency Alfvén mode is considered); for MEGA, in Ref. Bierwage et al. (2022) (where the confinement of fusion alpha particles during sawtooth crashes is discussed) and in Ref. Wang et al. (2024) (where the non-linear excitation of EP driven Geodesic Acoustic Mode (EGAM) in AUG tokamak is studied); and for HYMAGYC, in Ref. Vlad (2023) (where preliminary results of a non-linear benchmark among several codes were presented). Recently, also the code JOREK (Bogaarts 2022) has included a gyrokinetic module to describe the energetic particle population. Moreover, an example of the hybrid MHD-kinetic code is XTOR-K (Brochard 2020, 2025).

Within the EUROfusion E-TASC initiative (Litaudon 2022), a large effort has been undertaken to provide the European magnetically confined plasma community with up-to-date verified and validated numerical tools useful to study burning plasmas, both within the so-called TSVV (Theory, Simulation, Verification and Validation) tasks (in particular TSVV task 10 (Mishchenko 2023), dedicated to theory and simulations of burning plasmas, and a number of past EUROfusion's Enabling Research projects (such as "Multi-scale Energetic particle Transport in fusion devices" (MET Enabling Research Project 2020) and "Advanced Energetic Particle Transport" (Lauber 2024)). In this context, this review presents the results of a non-linear benchmark undertaken among several state-of-the-art codes available to study the self-consistent interaction of an EP population with shear Alfvén waves. This work is the natural continuation of the linear benchmark (Vlad 2021) study started as part of the EUROfusion 2021–2023 Enabling Research project "Advanced energetic particle transport models" (ATEP), and 2021–2025 Theory, Simulation, Validation and Verification project “Physics of burning plasmas” TSVV10. Studies of EP-driven modes with toroidal mode number $|n| = 1$ have been considered (Vlad 2021), in real magnetic equilibria and in regimes of interest for the forthcoming generation devices (e.g., ITER, JT-60SA, DTT). The codes considered for the linear benchmark were HYMAGYC (Fogaccia et al. 2016), MEGA (Todo 2006), and ORB5 (Lanti 2020), HYMAGYC being a MHD-Gyrokinetic code (the bulk plasma is represented by MHD equations, while the EP species is treated using the gyrokinetic formalism), MEGA being a MHD-Drift-Kinetic code (the bulk plasma is represented by MHD equations, while the EP species is treated using the drift-kinetic formalism, with the possibility of an ad-hoc gyroaveraging), ORB5 being a global electromagnetic gyrokinetic code (both bulk and EP species are treated using the gyrokinetic formalism); to which, now, the code XTOR-K (Brochard 2020, 2025) has been added, which is a non-linear kinetic-MHD code (the bulk plasma is described by a set of non-linear resistive two-fluid MHD equations, extended to include kinetic effects of multiple ion species with a fully kinetic PIC module). The so-called NLED-AUG reference case (Lauber 2016) has been considered during the linear benchmark, both for the peaked on-axis and peaked off-axis EP density profile cases, using its shaped cross-section version. Reference values for the equilibrium, here reconstructed using the high-resolution equilibrium code CHEASE (Lütjens et al. 1996), are: magnetic field and major radius at the magnetic axis $B_0[\mathrm{T}] \simeq 2.208$ and $R_0[\mathrm{m}] \simeq 1.666$, respectively, minor radius $a[\mathrm{m}] \simeq 0.483$, on-axis electron density $n_{\mathrm{e}0}[10^{20}/\mathrm{m}^3] \simeq 0.1716$, on-axis EP (“hot”) density (deuterons) $n_{\mathrm{h0,on-axis}}[10^{20}/\mathrm{m}^3] \simeq 0.0355$ (peaked on-axis case), and $n_{\mathrm{h0,off-axis}}[10^{20}/\mathrm{m}^3] \simeq 0.0046$ (peaked off-axis case, with an off-axis peak $n_{\mathrm{h-peak,off-axis}}[10^{20}/\mathrm{m}^3] \simeq 0.0215$ located at the radial position $s \approx 0.4$, with s being the square root of the normalized poloidal flux), and the bulk ion (deuteron) density obtained by the charge neutrality condition. Isotropic Maxwellian distribution function for the EP species has been considered with a constant-in-radius temperature $T_\mathrm{h}[\mathrm{MeV}] = 0.093$. A complete list of the equilibrium and physical parameters can be found in Table 3 of Ref. Vlad (2021). Some more details of the equilibrium considered will be also summarized in Sect. 2.

The linear benchmark (Vlad 2021) has been quite encouraging, in particular when considering peaked off-axis EP density profile: for this case, indeed, all the codes observe, for the nominal NLED-AUG reference case, a mode here identified as an EPM,[1] radially localized close to the magnetic axis, where the EP density profile is characterized by positive radial gradient, although with some spread in the linear growth-rate between HYMAGYC and MEGA, on one side, and ORB5 on the other, which exhibits a larger growth-rate value. When considering the case of peaked on-axis EP density profile, on the contrary, the differences between the three codes involved (HYMAGYC, MEGA, ORB5) were significant, if just looking

---

[1] Note that, because of its frequency localization almost within the shear Alfvén toroidal gap, in Ref. Vlad (2021) we named this mode a TAE; here we will refer to this mode, more properly, as an Energetic Particle Mode (EPM), because of its poloidal spectral composition being dominated by a single $m = 2$ Fourier component, instead of the characteristic m and $m + 1$ poloidal spectral composition of a TAE.

at the nominal NLED-AUG parameters: the first two codes were observing, as the most unstable EP-driven mode, a RSAE mode localized around mid-radius (where the minimum of the safety factor profile is located), whereas ORB5 were observing a TAE localized at the external part of the discharge. This discrepancy among the three codes was reconciled by considering scans of the EP drive, by varying either n_{h0} or T_{h0}, i.e., the on-axis EP density or temperature. From these scans, indeed, it was found that all three codes were able to observe both the RSAE and the external TAE, the dominance of one mode with respect to the other being characterized by different threshold values, likely to be related to the different dampings experienced by the three codes.

Here, it has been decided to extend the above-mentioned single n simulations to the non-linear saturation phase, keeping self-consistently the EP non-linearities on Alfvénic modes and particles themselves. Note that fluid non-linearities—such as wave–wave coupling effects—will be omitted in this study; thus, the focus will be on comparing wave-particle interactions effects across codes. Because of the results observed during the linear benchmark, it has been decided to choose, for this non-linear benchmark, the off-axis NLED-AUG case (all the codes observe, for this case, the same most unstable mode during the linear growth-rate phase). Moreover, when available, both simulations with only Finite Orbit Width (FOW) effects or including also Finite Larmor Radius (FLR) effects will be considered (it has to be reminded that only FOW effects were retained in the linear benchmark (Vlad 2021)). Note that in this non-linear benchmark we will present the results obtained by the various codes only for the single nominal case, thus without any scanning in parameters space: we are aware that this choice could limit the completeness of such a benchmark; nevertheless, we consider still valuable the presentation of such results that already required considerable effort, and we will reserve for future work the completion of such an exercise.

The paper is organized as follows: in Sect. 2 details of the NLED-AUG equilibrium considered will be presented together with some details on the parameters used by the various simulations. Then, in Sect. 3 the results obtained by the HYMAGYC code will be presented, in Sect. 4 the ones by the MEGA code, in Sect. 5 the ones by the ORB5 code, and in Sect. 6 the ones by the XTOR-K code. Finally, concluding remarks will be presented in Sect. 7.

2 Equilibrium and physical parameters

As announced in the Introduction, the equilibrium considered in this non-linear benchmark is the so-called NLED-AUG, originally proposed by Ph. Lauber within the EUROfusion Enabling Research Project NLED (Lauber 2016): the AUG shot considered is the #31213, at $t = 0.84$ s. Because of its EP pressure, the rich spectrum of experimentally observed instabilities and their non-linear interaction (Lauber 2018), the NLED-AUG test case poses an exceptional challenge to the numerical codes. Here, as in the linear benchmark already cited (Vlad 2021), we have considered a “variant” of the original NLED-AUG test case, that is, we have considered the fully shaped cross section version of this equilibrium (Lauber 2016), as described by a standard EQDSK file (see Fig. 1). Moreover, the equilibrium has been scaled using the equilibrium code CHEASE (Lütjens et al. 1996) to keep exactly the on-axis safety factor q_0 as tabulated in the EQDSK file itself, namely $q_0 \simeq 2.39897$: this choice results in a toroidal Alfvén gap fully open, when considering the reference bulk mass plasma density profile. Also, the experimental equilibrium has been transformed such to have both positive toroidal magnetic field and plasma current, when considering the equilibrium described by the so-called COCOS number (Sauter and Medvedev 2013), COCOS = 2, i.e. considering the coordinate system (R, Z, ϕ) used by CHEASE (Lütjens et al. 1996), and (s, χ, ϕ) used by HYMAGYC (here, R and Z are, respectively, the horizontal and vertical coordinates of the poloidal cross section of the torus, ϕ is the toroidal angle, s the square root of the normalized poloidal flux, χ the generalized poloidal angle).

Also, in Fig. 1 the electron, bulk-ion and energetic particle (both Deuterium) radial profiles are shown, for the so-called peaked off-axis EP density profile. As prescribed by the NLED-AUG test case, the bulk-ion density profile is defined as $Z_i n_i(s) = n_e(s) - Z_h n_h(s)$ (here n_i, n_e, n_h are the bulk ions, electrons, and EP densities, respectively, and $Z_i = Z_h = 1$ their electric charge numbers). For the purpose of this non-linear benchmark (as for the linear variant (Vlad 2021)) a Maxwellian

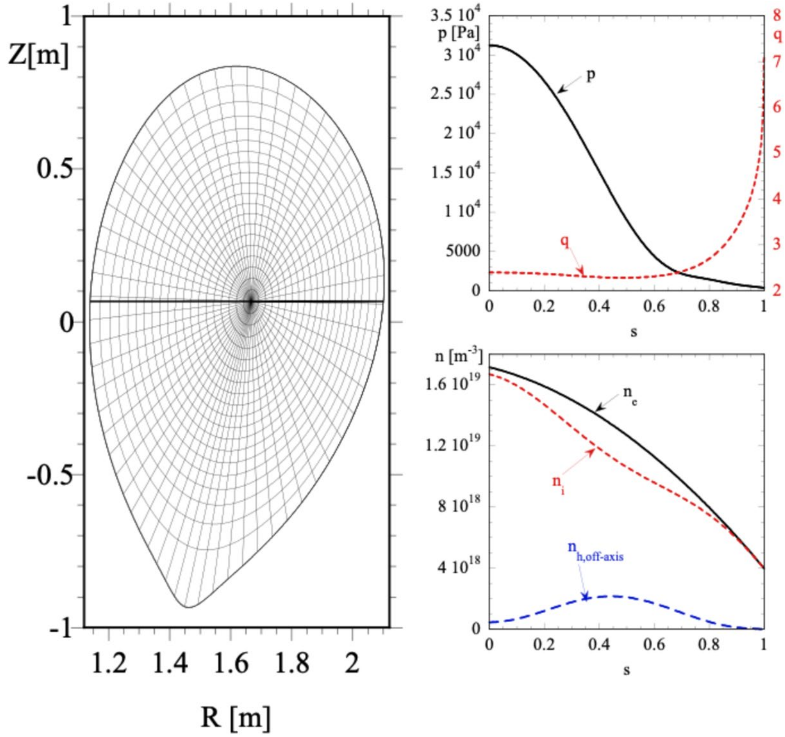

Fig. 1 Poloidal cross section (left), safety factor $q(s)$ and pressure $p(s)$ profiles (top right), and densities (bottom right) versus the square root of the normalized poloidal flux for the considered NLED-AUG test case

Table 1 NLED-AUG benchmark test case parameters for off-axis peaked EP density profile

Quantity	Value	Data definition/origin
B_{mag} [T]	2.20811798	EQDSK, magnetic field on the magnetic axis ($R = R_{\mathrm{mag}}$)
R_{mag} [m]	1.66599977	EQDSK, magnetic axis major radius
B_0 [T]	$B_0 = B_{\mathrm{mag}}$	Normalization coefficient for the magnetic field
R_0 [m]	$R_0 = R_{\mathrm{mag}}$	Normalization coefficient for the lengths
R_{geo} [m]	1.62	Geometric major radius $(R_{\mathrm{LCMS-max}} + R_{\mathrm{LCMS-min}})/2$
a [m]	0.48262	Minor radius $(R_{\mathrm{LCMS-max}} - R_{\mathrm{LCMS-min}})/2$
ϵ_0	0.297898	Inverse aspect ratio (a/R_{geo})
n_{e0} $[10^{20}/\mathrm{m}^3]$	0.171587	On-axis electron density
n_{h0} $[10^{20}/\mathrm{m}^3]$	0.00458182	On-axis EP density
$n_{\mathrm{h,max}}$ $[10^{20}/\mathrm{m}^3]$	0.0215	Maximum EP density at $s \approx 0.4$
n_{i0} $[10^{20}/\mathrm{m}^3]$	0.16700518	On-axis bulk ion density (from $Z_{\mathrm{i}} n_{\mathrm{i}} = n_{\mathrm{e}} - Z_{\mathrm{h}} n_{\mathrm{h}}$)
$n_{\mathrm{h0}}/n_{\mathrm{i0}}$	0.0274352	EP density/bulk ion density
$m_{\mathrm{i}}/Z_{\mathrm{i}}$	2/1	Bulk ion mass/charge (D) (in units of proton mass/electron charge)
$m_{\mathrm{h}}/Z_{\mathrm{h}}$	2/1	EP mass/charge (D) (in units of proton mass/electron charge)
$m_{\mathrm{h}}/m_{\mathrm{i}}$	1	Mass ratio (EP/bulk ion)
T_{h0} [MeV]	0.093	On-axis EP Temperature (constant on radius), Maxwellian distribution
v_{A0} [m/s]	8.32911×10^6	On-axis Alfvén velocity: $v_{\mathrm{A0}} = 2.18 \times 10^6\, B_{\mathrm{mag}}[\mathrm{T}]/\sqrt{m_{\mathrm{i}} n_{\mathrm{i0}}[10^{20}/\mathrm{m}^3]}$
τ_{A0} [s]	2.00021×10^{-7}	On-axis Alfvén time: $\tau_{\mathrm{A0}} \equiv R_0/v_{\mathrm{A0}}$
ω_{A0} [rad/s]	4.99947×10^6	$\omega_{\mathrm{A0}} = 1/\tau_{\mathrm{A0}}$
$v_{\mathrm{h,th0}}$ [m/s]	2.1111×10^6	$v_{\mathrm{h,th0}} \equiv \sqrt{T_{\mathrm{h0}}/m_{\mathrm{h}}} = 9.79 \times 10^6 \sqrt{T_{\mathrm{h0}}\,[\mathrm{MeV}]/m_h}$
$v_{\mathrm{h,th0}}/v_{\mathrm{A0}}$	0.253461	On-axis EP thermal velocity/on-axis Alfvén velocity
Ω_{h0} [rad/s]	1.057688×10^8	On-axis EP gyrofrequency: $\Omega_{\mathrm{h0}} = 9.58 \times 10^7 Z_{\mathrm{h}} B_0\,[\mathrm{T}]/m_{\mathrm{h}}$
ρ_{h0} [m]	0.0199221	On-axis EP Larmor radius $\rho_{\mathrm{h0}} = v_{\mathrm{h,th0}}/\Omega_{\mathrm{h0}} = 0.102\sqrt{m_{\mathrm{h}} T_{\mathrm{h0}}[MeV]}/(Z_{\mathrm{h}} B_0[T])$
ρ_{h0}/R_0	0.011958	On-axis EP Larmor radius/R_0
ρ_{h0}/a	0.041279	On-axis EP Larmor radius/a

distribution function has been assumed for the EPs with a constant in radius temperature profile $T_{\mathrm{h}}(s) = 0.093$ [MeV]. Since this distribution function is not an equilibrium one its evolution would lead to an immediate relaxation even in the initial (essentially unperturbed) phase. To avoid such relaxation, thus maintaining the correspondence of the initial parameters and profiles to the experimental NLED-AUG ones, the three codes HYMAGYC, MEGA and ORB5 solve the δF form of the Vlasov equation in which the term containing the scalar product of the unperturbed velocities in phase space and the corresponding gradients of the initial distribution function is suppressed. A summary of the physical parameters for the NLED-AUG equilibrium, in its peaked off-axis variant, are reported in Table 1, for the convenience of the reader.

3 Non-linear HYMAGYC simulations

This section presents the results obtained by HYMAGYC. HYMAGYC (Fogaccia et al. 2016) is a hybrid MHD-gyrokinetic code suitable to study EP-driven modes in general high-β axisymmetric equilibria, (β being the ratio of the plasma pressure to the magnetic pressure), with perturbed electromagnetic fields (electrostatic potential φ and vector potential $\mathbf{A}$) fully accounted for. The thermal plasma is described by linear, full, resistive MHD equations in arbitrary axis-symmetric equilibria. The MHD module originates from the full, linear, resistive MHD code MARS (Bondeson et al. 1992), transformed from an eigenvalue solver to an initial value one, using a fully implicit (backward Euler) finite difference time discretization scheme (see appendix A.2 in Vlad et al. (1999)). Fourier decomposition in the generalized poloidal (χ) and toroidal (ϕ) angles is also used, together with generalized finite element method along with the Tunable Integration Method (Bondeson and Fu 1991) for the discretization in the radial-like coordinate $s = \sqrt{|\psi - \psi_0|/|\psi_{\text{edge}} - \psi_0|}$ (with ψ the equilibrium poloidal flux function, and ψ_0 and ψ_{edge}, respectively, the value of ψ on the magnetic axis and on the last closed magnetic surface). The generalized poloidal angle χ used in HYMAGYC is chosen in the CHEASE code (when preparing the equilibrium quantities necessary to the MHD solver of HYMAGYC) by imposing the Jacobian of the transformation from the flux coordinates (s, χ, ϕ) to the Cartesian coordinates the following form Grimm et al. (1983): $J \propto R^\alpha |\nabla\psi|^\mu$, with α, μ integers. In the following simulations, $\alpha = 1$, $\mu = -1$ has been assumed, which corresponds to the so-called *equal arc length* coordinate system. The EP population is described by the non-linear gyrokinetic Vlasov equation, solved by particle-in-cell (PIC) techniques, and expanded up to order $O(\epsilon^2)$ and $O(\epsilon\, \epsilon_B)$, ϵ being the gyrokinetic ordering parameter $\epsilon \sim \rho_{\text{h}}/L_n$ and $\epsilon_B \sim \rho_{\text{h}}/L_B$, with ρ_{h} the EP Larmor radius, L_n and L_B the characteristic equilibrium plasma density and magnetic-field nonuniformity length scales, respectively. As $L_n/L_B \ll 1$, $O(\epsilon_B^2)$ terms are neglected (further details can be found in Ref. Vlad (2021); in "Appendix Appendix A" the equation of motion considered for the EP population in this paper for the code HYMAGYC are explicitly presented). The standard δf method for the EP distribution function is used, i.e., the EP distribution function is written as $F_{\text{h}} = F_{\text{h},0} + \delta f_{\text{h}}(t)$, with $F_{\text{h},0}$ the initial, time-independent EP distribution function, and the Vlasov equation is solved for $\delta f_h(t)$. The coupling between MHD and EPs is obtained by adding to the MHD momentum equation a term proportional to $\nabla \cdot \Pi_k$ (Park 1992) (Π_k being the EP stress tensor). Flux coordinate system (s, χ, ϕ) is used. The MHD solver can consider finite resistivity η and finite adiabatic index Γ, but no viscosity. In the following simulations, a value of normalized resistivity given in terms of the inverse of the Lundquist number $S^{-1} = 5 \times 10^{-7}$ (with $S \equiv \mu_0 R_0 (v_{\text{A0}}/\eta)$, with v_{A0} the on-axis Alfvén velocity), and $\Gamma = 5/3$ are used. Regarding the MHD module a equidistant radial mesh with 180 grid points has been used, and a poloidal Fourier spectrum $m = [-3, 13]$, for the considered $n = -1$ toroidal mode. Regarding the gyrokinetic module, the numerical markers describing the EP distribution function are evolved in a 3D flux coordinate space (s, χ, ϕ) using a $N_s \times N_\chi = 180 \times 120$ grid points in the (s, χ) space and a gridless finite-size approach (Vlad et al. 2001) along

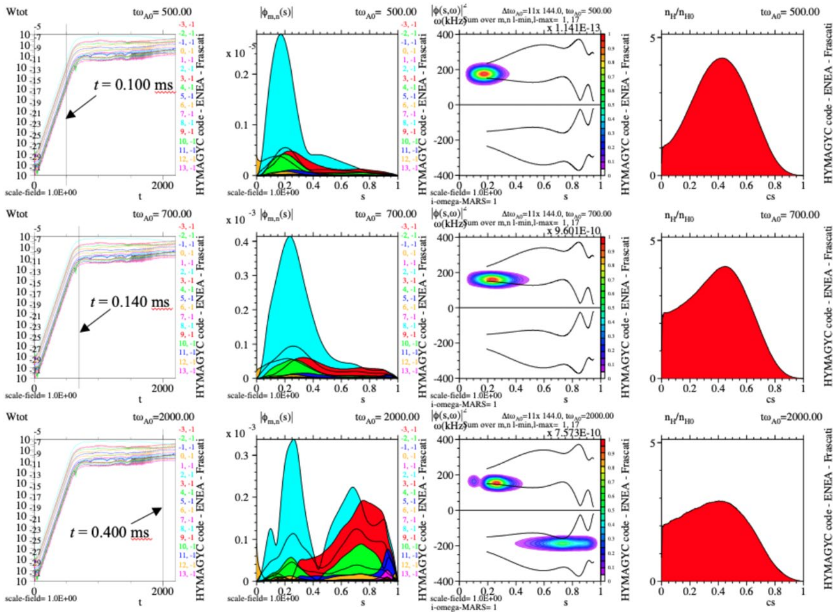

Fig. 2 Non-linear simulation of HYMAGYC (FLR effects retained, toroidal mode number $n = -1$). Volume-integrated energy (a.u.) of the Fourier components versus time (first column), radial profiles of the Fourier components of the electrostatic potential (a.u., second column), its frequency spectra (third column), EP density profiles (normalized to its on-axis value at $t = 0$, fourth column) are shown for three characteristic times during simulation: linear phase (first row), early saturated phase (second row), and long saturated phase (third row). In the third column plots (frequency spectra) black solid curves represent the shear Alfvén continua (Falessi et al. 2019)

the ϕ direction; typically, we use a number of simulation particles per cell $N_{\mathrm{part/cell}} \equiv N_{\mathrm{ppc},s} \times N_{\mathrm{ppc},\chi} \times N_{\mathrm{ppc},\phi} = 64$, with a number of cells along ϕ conventionally fixed to $N_\phi = 8$, thus considering a total number of EP markers $N_{part} = 11{,}059{,}200$. (see Ref. Vlad (2021) for more details). Note that the numerical parameters used to run HYMAGYC in these simulations have been checked for convergence assuring that the physical results are not (reasonably) dependent on them. Such practice has been ensured for all the codes included in this benchmark.

As an example of the results obtained, in Fig. 2 three representative times of a $n = -1$ non-linear simulation using HYMAGYC are presented when retaining FLR effects, and EP stress term computed using (s, χ) coordinates: for each of the three time snapshots (different rows), the volume integrated energy of the Fourier components (first frame), the radial profiles of the Fourier components of the electrostatic potential (second frame), its frequency spectra (third frame), and the Energetic Particles density profile (fourth frame) are shown.

Note that in the frequency spectra frames, here and in the following figures showing such quantity, also the shear Alfvén continuous spectra are shown for reference, as obtained by the FALCON code (Falessi et al. 2019) in the limit of slow-sound approximation (Falessi et al. 2020); acoustic Alfvén continua as obtained

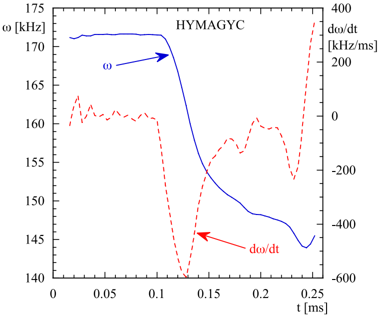

Fig. 3 Frequency chirping (blue, solid curve) and rate of chirping (red, dashed curve) for the EPM mode shown in the HYMAGYC simulation of Fig. 2)

by FALCON, although present in the system, are not shown for the sake of clarity of the figures. The first snapshot refers to the linear phase (normalized time $t\omega_{\mathrm{A0}} = 500 \rightarrow t \simeq 0.100\,\mathrm{ms}$, first row), the second one to the early saturated phase ($t\omega_{\mathrm{A0}} = 700 \rightarrow t \simeq 0.140\,\mathrm{ms}$, second row), and the third one to the long saturated phase ($t\omega_{\mathrm{A0}} = 2000 \rightarrow t \simeq 0.400\,\mathrm{ms}$, third row) (here the time is normalized to the inverse of the on-axis Alfvén time $\omega_{\mathrm{A0}} \equiv 1/\tau_{\mathrm{A0}} = v_{\mathrm{A0}}/R_0 = 4.99947 \times 10^6 s^{-1}$). It is notable to observe that the most unstable mode during linear growth phase is a EPM radially located close to the magnetic axis, in the region where the EP density radial profile exhibits a positive radial gradient; as soon as the mode enters the saturation phase ($t\omega_{\mathrm{A0}} \simeq 700$) the mutual interaction between the Alfvén mode and the EPs makes the EP density profile to be modified, filling the hollow region toward the magnetic axis while reducing the radial gradient. Meanwhile, the mode frequency chirps downward, following the lower Alfvénic continuum of the toroidal gap as the mode peak shifts a little outward (see Fig. 3 where the frequency chirping at saturation of the EPM is shown, together with the rate of frequency chirping).

At longer time ($t\omega_{\mathrm{A0}} \simeq 2000$) a TAE localized in the external part of the toroidal gap also appears, with frequency opposite in sign w.r.t. the most unstable mode observed during the linear phase, and being driven by the EPs located in the external region of the discharge, where their radial density profile is characterized by a negative radial gradient. No chirping of this outer TAE is, indeed, observed. Evidence of inward EP transport (Lauber 2020) has, indeed, been observed in AUG discharges with off-axis peaked EP density profile, similar to the one considered in this benchmark (note, however, that this evidence should not be considered as a validation between the results of this benchmark and the experiment, because of the various differences among them (just to mention one, the isotropic Maxwellian EP distribution function with $T_{\mathrm{h}} = 0.093$ [MeV] used in the simulations and the anisotropic slowing down in the experiment with a beam energy $E_{\mathrm{beam}} = 0.093$ [MeV])).

The EP density profiles at different simulation times are shown in Fig. 13, top row, left frame, for the same simulation shown in Fig. 2. Several features can be observed from the figure. The initial EP density profile (black thick curve labelled “0”) rapidly relaxes due to EP first orbit losses – i.e., particles initialized in the system that have unconfined, unperturbed orbits ($t = 0 - 0.020$ ms). Note that in HYMAGYC, EPs that cross the last closed magnetic surface are considered lost and are not re-injected into the system. During the linear growth phase ($t = 0.020 - 0.120$ ms), the

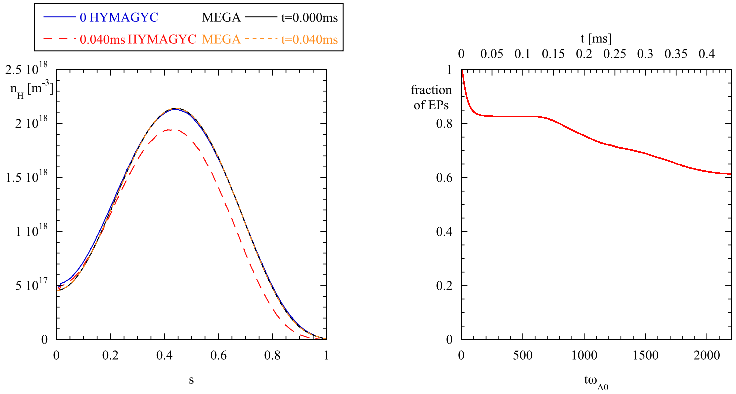

Fig. 4 (Left) EP density profile for HYMAGYC: $t = 0$ [ms] (blue curve) and "relaxed" $t = 0.040$ [ms] (red curve); compared with EP density profile for MEGA $t = 0$ [ms] (black curve) and at $t = 0.040$ [ms] (orange curve); note that the two curves corresponding to the MEGA simulation almost overlaps one to the other. (Right) Fraction of EPs versus time for the HYMAGYC simulation shown in Fig. 2

EP density profile remains almost constant. As the system enters the early non-linear saturation phase ($t = 0.140 - 0.200$ ms), the EP density profile is strongly modified. In particular, the hollow central region near the magnetic axis becomes "filled", while the peak at mid-radius decreases simultaneously. Subsequently, during the late non-linear saturation phase ($t > 0.200$ ms), the EP density profile shows only minor changes. A slight broadening appears in the outer region as the subdominant, external TAE becomes dominant ($t > 0.300$ ms), which is also indicated by a small increase in the energy time traces shown in Fig. 2. Eventually, the system reaches saturation ($t > 0.400$ ms). Regarding the initial relaxation of the EP density profile occurring in HYMAGYC, we plot in Fig. 4 (left) a comparison between the EP density profile for HYMAGYC and MEGA at $t = 0$ [ms] and $t = 0.040$ [ms], where the differences are apparent. We also show in Fig. 4 (right) the time history of the total number of physical EPs (normalized to its initial value) in the HYMAGYC simulation: almost 15% of the EPs are lost as first orbit losses ($t = 0. - 0.040$ ms); during the linear growing phase the number of particles within the simulation domain is almost constant ($t = 0.040 - 0.140$ ms), while from the beginning of the saturation phase to the end of the simulation another 20% of particles are lost.

To better illustrate the time traces of the different Fourier components considered in the simulation, we show in Fig. 5 the same plots shown in Fig. 2, left column, both in logarithmic and linear scale, in particular to appreciate more clearly the amplitude behaviour during the saturated phase; also the total energy (kinetic plus magnetic, summed over all the poloidal Fourier components) is shown, in black. In the linear scale plot (Fig. 5, right) it is clearly observable that first the EPM saturates, dominated by the $m = 2$ component, with few overshooting (cyan colored curve); later on, the external TAE dominated by the $m = 2, 3$ components take over (cyan and red colored curves) (see also Fig. 2, third column plots).

It is instructive to analyze the power exchange P between the EPs and wave, to gain some insight on which part of the EP population is responsible for driving the

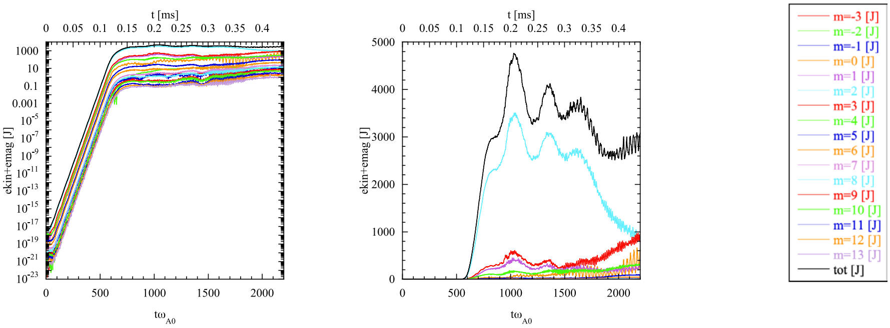

Fig. 5 Non-linear simulation of HYMAGYC (FLR effects retained, toroidal mode number $n = -1$). Volume-integrated energy (Joule units) of the Fourier components versus time in logarithmic (left) and linear (right) scales, respectively. Black curves represent the total energy (summed over all the poloidal Fourier components). The labels and color codes of the curves are common to both boxes. Note that the left panel of this figure is equal to the ones already shown in Fig. 2, first column

system. In Fig. 6 the power exchange during the linear growing phase is shown (normalized time $t\omega_{A0} = 500 \rightarrow t \simeq 0.100\,\mathrm{ms}$). In the top row of Fig. 6 the contributions of all the EPs are summed together and plotted after projecting, respectively, on the planes (U, M), (M, s) and (U, s) (U is the normalized (to thermal EP velocity) EP parallel velocity, M is the normalized (to T_h/Ω_{h0}) magnetic moment), whereas in the bottom row only the trapped EPs are retained (light green to red color colors represent positive contribution, i.e., EPs drive the wave, whereas cyan to violet represent negative contribution, i.e., EPs damp the wave). Most of the drive is given by co-passing and counter-passing EPs, which are radially located in the inner half of the plasma discharge, where the EP density profile exhibits a positive radial gradient (see Fig. 1): this drive is responsible for the growing of the dominant EPM which is radially located close to the magnetic axis, as observed in Fig. 2. A weaker, subdominant contribution is also present, which is clearly observed in the second row of Fig. 6, where only the trapped EP contribution is shown (typically one order of magnitude smaller then the contribution coming from co-passing and counter-passing EPs). This contribution is clearly localized in the external region of the plasma column, where the EP density profile exhibits a negative radial gradient (see Fig. 1), and it is likely to be responsible for the subdominant TAE mode which emerges in the late saturated phase, once the dominant internal EPM has been weakened by displacing the EP density profile (see Fig. 2, bottom row).

Regarding the computation of the EP stress tensor and its divergence components, HYMAGYC has been recently updated to be able to compute them also using a Cartesian (R, Z) coordinate system in the poloidal plane, besides the usual (s, χ) one. Indeed, relative modest differences are observed between the two methods when considering the linear phase of the simulations, but the evaluation of the EP stress tensor using the (s, χ) coordinates during the non-linear saturation phase could often be prone to the excitation of short-scale perpendicular perturbations, which can eventually lead to numerical instabilities and prevent the simulation of a long saturated phase. This is particularly true when only FOW effects are considered,

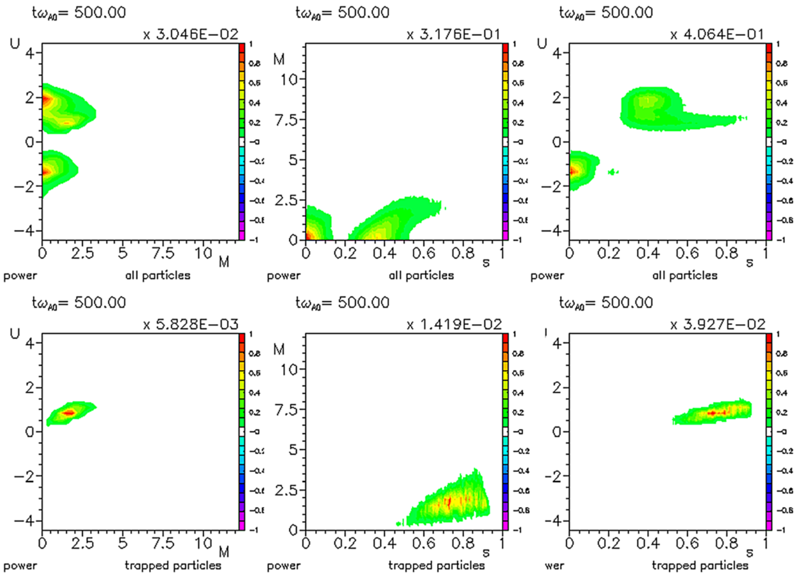

Fig. 6 Power exchange $P(M, U, s)$ between energetic particles and wave, after integration on the toroidal and generalized poloidal angles: projections on the planes (U, M) (first column), (M, s) (second column), and (U, s) (third column). In the top row, the total power exchange, which includes all the EP contribution, is shown, whereas in the bottom row only the power exchange given by the trapped particles is shown (which is approximately one order of magnitude smaller then the total contribution). Positive contribution means the EPs drive the mode

while the intrinsic spatial averages introduced by FLR effects seem to favorite the avoidance of this unwanted phenomenology.

To illustrate the intrinsic filter of unrealistic short scale oscillations as arising by the introduction of a Cartesian (R, Z) coordinate system to compute the EP stress tensor and its divergence components, we show in Fig. 7 how the poloidal spectrum of the MHD total energy (kinetic plus magnetic) varies as the dimensions of the (R, Z) meshes are reduced.

Three different couples of values are considered for the $N_R \times N_Z$ grid points: $N_R \times N_Z = 121 \times 121$, $N_R \times N_Z = 181 \times 181$, $N_R \times N_Z = 361 \times 361$; moreover, results are presented both during the linear growth phase and during the long saturated phase of an FOW simulation. Poloidal spectra are peaked at $m = 2$ poloidal component during linear phase, and at $m = 3$ poloidal component during the long saturated phase, as can be also observed by the radial profiles of the e.s. perturbations in Fig. 2 (note, however, that the simulation shown in Fig. 2 retain also FLR effects). During the linear growing phase, the tails of the spectra, far away from the dominant poloidal component, strongly decrease as the mesh sizes are reduced, resulting in stable and much less noisy simulations. During the saturated phase the tails of the spectra tend to decay less, as can be reasonably expected, but the filter effect of smaller Cartesian grid is still clearly observable.

In Table 2, first two rows, the growth-rates and real frequencies, as obtained in the linear phase of HYMAGYC simulations, are compared as FOW only, or also

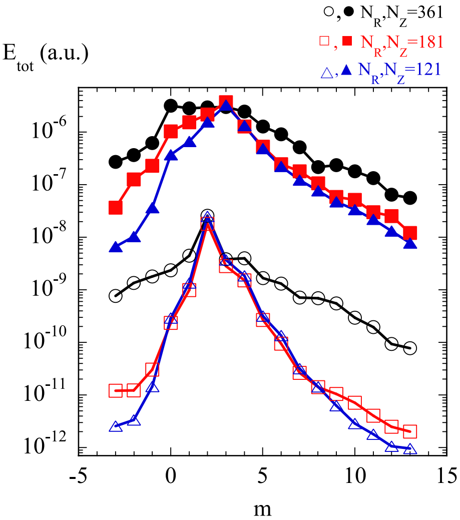

Fig. 7 HYMAGYC simulations: poloidal spectra of the MHD total energy (kinetic plus magnetic) as the dimensions of the (R, Z) grid are varied (circles refer to $N_R \times N_Z = 121 \times 121$, squares to $N_R \times N_Z = 181 \times 181$, triangles to $N_R \times N_Z = 361 \times 361$), during linear (three lower curves, open symbols) and saturated phases (three upper curves, filled symbols)

Table 2 Growth-rates and real frequencies in linear phase considering Finite Orbit Width only (FOW) or also Finite Larmor Radius effects (FLR), for: HYMAGYC with EP stress tensor computed using (s, χ), or (R, Z) coordinate systems, MEGA, and ORB5

Code	FOW		FLR	
	γ [s^{-1}]	$\omega/(2\pi)$ [kHz]	γ [s^{-1}]	$\omega/(2\pi)$ [kHz]
HYMAGYC (s, χ)	174,606	180.02	199,841	171.51
HYMAGYC (R, Z)	231,090	162.42	215,570	163.00
MEGA	218,616	171.43	170,247	157.00
ORB5	348,489	127.09	286,400	145.24

FLR effects, are retained, and as (s, χ) or (R, Z) (with $N_R \times N_Z = 121 \times 121$ grid points) coordinate systems for computing the EP stress tensor are considered: some differences are indeed observed in the linear growth phase for the different cases, although quite modest, and, apart of the "FOW, (s, χ)" case which is numerically unstable in the long saturated phase, similar qualitative non-linear behaviour is observed for all the other cases.

4 Non-linear MEGA simulations

This section presents the results obtained by the MEGA code. MEGA (Todo 2006) is a hybrid MHD-Drift-Kinetic code where the bulk plasma is described using non-linear full MHD equations, and the EPs are described by the drift-kinetic equation, with the possibility of an ad-hoc gyroaveraging. The energetic ion contribution is included in the MHD momentum equation as the EP current density. The standard δf method is used for evolving the EP distribution function. The electromagnetic field is given by the standard MHD description, for this benchmark. Resistivity, viscosity and diffusion terms are included in the equations. Normalized resistivity $S^{-1} = 5 \times 10^{-7}$ and normalized viscosity $\nu_{\mathrm{norm}} \equiv \nu/(R_0 v_{\mathrm{A0}}) = 5 \times 10^{-7}$ are used here; moreover, an adiabatic index $\Gamma = 5/3$ is also used in the MHD solver, similarly to HYMAGYC. Note that (R, ϕ, Z) coordinates are used for solving the equations, with $N_R \times N_\phi \times N_Z = 128 \times 16 \times 256$ grid points, while flux coordinates are considered for the result analysis. The number of marker particles used to describe the EP distribution function is $N_{part} = 8{,}388{,}608$, i.e., $N_{\mathrm{part/cell}} = 16$. The output of MEGA is in flux coordinates space (s, ϕ, θ), and the Fourier components are chosen by $n = [-1, 0, 1]$ and $m = [0 - 64]$.

In Table 2, third row, we compare the growth-rates and real frequencies derived from the linear phase of MEGA simulations. These comparisons are made considering cases with FOW effects (which for MEGA code has to be intended as Drift-Kinetic, DK) or including FLR effects (i.e., DK plus an ad-hoc N-point averaging). We observe that the linear growth-rates are lower when FLR effects are considered, compared to cases retaining only FOW effects. These findings align with results from HYMAGYC simulations under EP stress tensor calculations in (R,Z) coordinates and with findings from ORB5 simulations. However, there are notable differences in the real frequency between FOW and FLR scenarios across the HYMAGYC, MEGA, and ORB5 simulations. Specifically, MEGA simulations demonstrate a reduced real frequency in the FLR simulation, HYMAGYC simulations exhibit closely matched real frequencies, and ORB5 simulations show an increased real frequency in the FLR case.

In Fig. 8, we present the effects of retaining FLR in the reference NLED-AUG EP case, which has an off-axis peak. This presentation

includes three time snapshots (organized in different rows), showcasing the energy evolution of the $n = 1$ mode (first column), the radial profiles of the Fourier components of the normalized electrostatic potential (second column), its frequency spectra (third column), and the EP density profiles (fourth column). There is a qualitative agreement observed between the MEGA and HYMAGYC results. Notably, both codes reveal the emergence of an external TAE during the prolonged saturated phase, rotating in the opposite direction to the dominant linear mode. Concurrently, in the non-linear evolution phase, the linearly driven unstable EPM mode exhibits downward frequency chirping, and the mode peak shifts slightly outward, a phenomenon also observed in HYMAGYC simulations. Interestingly, the energy evolution indicates that the appearance of the external TAE coincides with a secondary growth stage in simulations from both codes. In the MEGA simulation, the onset of the second growth stage occurs approximately 0.1 ms following the initial saturation phase. This contrasts with the HYMAGYC simulations, where the second growth phase begins after a more extended delay, exceeding 0.2 ms post the first saturation. In Fig. 9 we show the plots of the volume integrated energy versus time both in logarithmic and linear scales, to better appreciate the dynamics at saturation: a level of the volume-integrated energy considerably lower than that observed in the HYMAGYC simulation (see Fig. 5) is indeed observed (a factor ≈ 15 for the first "overshooting").

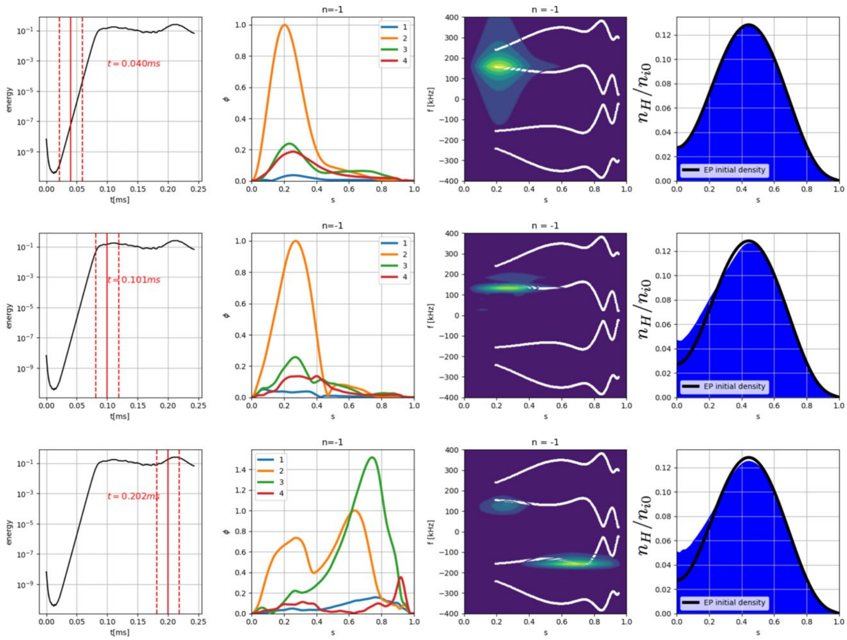

Fig. 8 Non-linear simulation of MEGA. Volume integrated energy of the $n = 1$ perturbation versus time (first column), radial profiles of the Fourier components of the electrostatic potential (second column), its frequency spectra (third column), and the EP density profiles (normalized to the on-axis bulk ion n_{i0}, fourth column) are shown for three characteristic times during simulation: linear phase (first row), early saturated phase (second row), and long saturated phase (third row). In the third column plots (frequency spectra) white solid curves represent the shear Alfvén continua (Falessi et al. 2019)

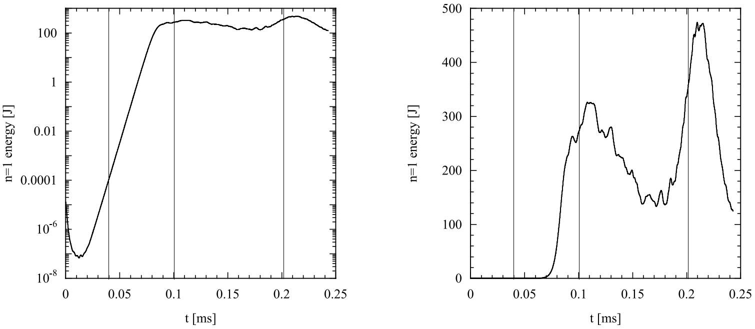

Fig. 9 Non-linear simulation of MEGA (FLR effects retained). Volume integrated energy (Joule units) of the Fourier components versus time in logarithmic (left) and linear (right) scales, respectively

Regarding the evolution of the EP density profile, as illustrated in the fourth column of Fig. 8 and the top row, right frame of Fig. 13, the MEGA simulation does not exhibit an initial relaxation in the EP density profile. During the non-linear mode evolution, the simulation reveals a “filling” effect in regions close to the axis, whereas the reduction in the mid-radius region is significantly less pronounced compared to the HYMAGYC simulation. This disparity could have been attributed to the lower level of perturbation amplitude observed in the MEGA simulation, w.r.t. the HYMAGYC one: to check this eventuality a simulation with a slightly reduced EP drive (reduced n_{h0}) has been performed: the non-linear relaxation in the HYMAGYC simulation with a lower value of n_{h0} is, as expected, smaller than the one observed for the nominal case, but still much larger than what observed in the MEGA simulation in the early saturated phase. Indeed, this first non-linear benchmark demonstrates a qualitative agreement among codes, showing similarities. However, numerous details are absent and require further investigation. Simultaneously, no conspicuous redistribution is observed in the outer regions of the EP density profile. This lack of redistribution and the consequent persistence of a steeper gradient in the EP density profile, as opposed to the more relaxed profile seen in the HYMAGYC simulations, may explain this earlier onset of the external TAE mode.

5 Non-linear ORB5 simulations

This section presents the results obtained by the ORB5 code. ORB5 (Lanti 2020) is a global, non-linear, electromagnetic, PIC code which solves the gyrokinetic Vlasov–Maxwell system of equations. It can take into account collisions and heat, particle and momentum sources (which are neglected in the present work). The distribution function of each species "sp" is composed of a time-independent background component $F_{0,sp}$ and a time-dependent part δf_{sp}. The latter is represented by sample of numerical particles (markers), which are pushed with a 4th-order Runge–Kutta scheme along the trajectories defined by the equation of motion of the gyrocenter characteristics $(\vec{R}, v_{\|}, \mu)$. In ORB5, straight field-line coordinates are used: (s, θ^*, ϕ). The radial coordinate, s, is the same used by the code HYMAGYC, and defined before. The angular coordinates are the toroidal angle ϕ and the poloidal magnetic angle $\theta^* = q^{-1}(s)\int_0^\theta [(\vec{B}\cdot\nabla\phi)/(\vec{B}\cdot\nabla\theta')]d\theta'$, where $q(s)$ is the safety factor profile and θ the geometric poloidal angle. The equations of motion are coupled with the field equations: the Poisson equation (in the quasi-neutrality limit) and the parallel Ampère's law. These are solved using finite elements (typically cubic B-splines) on a grid $(N_s, N_{\theta^*}, N_\phi)$. A field-aligned Fourier filter is used (Jolliet 2007). At each radial grid point s, for each toroidal mode n, only the poloidal modes $m \in [-n \cdot q(s) \pm \Delta m]$ are retained, being Δm the width of the retained poloidal modes. The equations are solved through a mixed-variable pullback algorithm to mitigate the so-called cancellation problem (Mishchenko 2019). The number of grid points for ORB5 simulations for the coordinate system (s, θ^*, ϕ) is $N_s \times N_{\theta^*} \times N_\phi = 2000 \times 144 \times 48$ and the number of markers M, respectively, for bulk ions, EPs, and electrons are $M_{\mathrm{i}} = M_{\mathrm{EPs}} = 3 \times 10^7$, and $M_{\mathrm{e}} = 12 \times 10^7$. We would like to emphasize that the results shown here are inserted in a chain of studies presented in previously published papers dedicated to investigate the Alfvén mode dynamics in the NLED-AUG case. In particular, in Ref. Vannini (2022), a

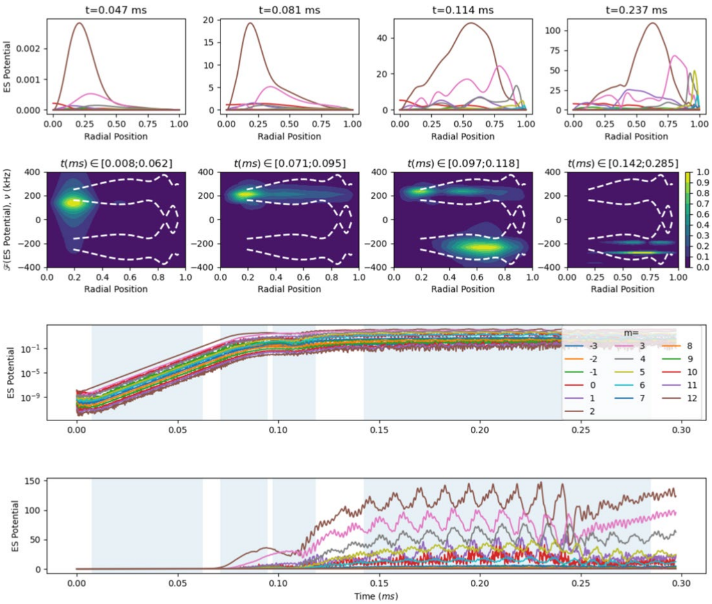

Fig. 10 Non-linear simulation of ORB5, retaining FLR effects: radial profiles of the Fourier components of the electrostatic potential at different times of the simulations (first row). its frequency spectra (second row), and the time evolution of the maximum against the radial position of the electrostatic potential (in logarithm scale (third row) and linear scale (fourth row)). Note that the four shaded time intervals in the third and fourth row plots correspond to the time interval used to Fourier transform in time the ES potential (second row plots). In the second row plots (frequency spectra) white dashed curves represent the shear Alfvén continua (Falessi et al. 2019)

convergence test for the NLED-AUG case was presented. The results here presented are based on such previously conducted convergence tests.

ORB5 simulations in the linear phase are characterized by higher growth-rates and lower real frequencies, w.r.t. HYMAGYC and MEGA results, both for FOW and FLR cases (see Table 2, fourth row). The lower plot in Fig. 10 shows the time evolution of the maximum against the radial position of the electrostatic potential for the poloidal mode number given in the legend. Four time windows have been selected (blue time regions). In the indicated time windows, the temporal Fourier transform of the signal has been calculated (first row of Fig. 10) and the mode structure at a selected time within the corresponding time window is shown (second row of Fig. 10). Consistent with studies presented in previous published work (Vannini 2022), the dominant Alfvén Mode in the linear phase (first temporal window) appears to be an EPM dominated by the Fourier component (m,n)=(2,1) and peaking around the radial position s=0.2. Proceeding inside the non-linear phase and especially in the third temporal window selected, we observe that the scalar potential Fourier component (m,n)=(3,1) grows and reaches an amplitude comparable to that of the dominant (m,n)=(2,1). Furthermore, looking at the frequency variation, it is clear that the EPM chirps up and reaches the TAE gap:

note that the chirping direction is opposite to the one observed by both HYMAGYC (see Sect. 3) and MEGA (see Sect. 4). In addition, during the long saturation phase, the appearance of the external TAE, rotating in the opposite direction to the dominant linear mode, is observed. The formed mode is no longer located only in the central region, but also in the outer region. This also affects the EP transport, as shown in Fig. 13, where the EP density profiles are given in units m^{-3}. There we observe the "filling" of the region close to the axis and the decrease of the density in the mid-radius region where the TAE is located. One interesting observation from Fig. 10 is the significant radial expansion of the EPM mode structure in the nonlinear stage, overlapping with the external TAE mode. A similar effect is also seen in the HYMAGYC (see Fig. 2) and MEGA (see Fig. 8) results, though less prominently. This feature is an example on how the inner core region, characterized by weak magnetic shear and low-frequency Alfvénic activity, can be connected to the outer core region, with typically finite magnetic shear, resulting in possible enhancement of the EP transport from the core toward the edge (see, e.g., Ref. Wang et al. (2019)). The evolution of the EP density profile computed with ORB5 is qualitatively similar to that of XTOR-K, although the flattening is a bit stronger for the latter. We note that HYMAGYC results also show a flattening of n_h, however here accompanied by an overall decrease of EP density, which seems to indicate larger losses at the edge. The MEGA results, on the other hand, have a much less pronounced evolution of the EP density. These differences will be addressed in future works. In particular, they may be related to the different implementations of particle boundary conditions at the edge.

6 Non-linear XTOR-K simulations

This section presents the results obtained by the XTOR-K code (Brochard 2020, 2025). XTOR-K is a global hybrid fluid/kinetic code which solves a 2-fluid set of equations coupled with a PIC "full-f" method and bulk ion and electron temperature evolutions. The fluid and the kinetic equations are coupled together with a kinetic pressure term in the perpendicular equation of motion. The time evolution is solved by a method combining self-consistently a fully implicit pre-conditioned Newton-Krylov method for the fluid fields combined with a Boris-Buneman scheme for the kinetic ions. Both time advances are nested inside a Picard iteration for every fluid time step, which ensures simultaneous convergence of fluid and kinetic parts. The velocity moments are extracted from the kinetic module at the end of every time advance of the fluid part inside this iteration. The code uses radial domain decomposition in the fluid section and domain cloning or domain decomposition in the kinetic section. The latter is required if binary collisions are taken into account. The particle distribution f is given by a set of markers characterized by the charge, the mass and the local density of the kinetic ions. In the present simulations we use 24 particle integration steps per kinetic ion cyclotron gyration and 16 particles time steps per fluid time step. Quasi-neutrality is imposed at every fluid time step by $n_\mathrm{e} = Z_\mathrm{i} n_\mathrm{i} + \Sigma_k (Z_k n_k)$. The discretization mesh in the fluid part is toroidal ($s = \sqrt{\psi}, \theta, \phi$) where ψ is the initial equilibrium poloidal magnetic flux and θ

the geometric polar angle. XTOR uses FFT's in both angular directions and radial linear finite differences in the fluid part. In addition, it uses FFT's toroidally and a Cartesian coordinates in the small section of the torus in the kinetic part. The number of grid points in the presents simulations are $(N_s, N_\theta, N_\phi) = (204, 64, 8)$ and $(N_R, N_Z, N_\phi) = (400, 400, 8)$ in the kinetic module, where N_θ and N_ϕ are the number of Fourier modes. The simulation starts with 307.2×10^6 markers. For the present study, the fluid model is restricted to ideal MHD with a very small viscosity. Moreover, after every fluid time step only the $n = 1$ component of the fluid field increments is filtered out and retained. This was done to approach, at best, the simulations with the other codes. Usually, XTOR includes all toroidal components on the fluid and the kinetic side, including the time evolution of $n = 0$. The initial conditions of the NLED test case presented here are given by a set of points for the boundary and the polynomial profiles given by Lauber (2016) for q, n_i, T_i, T_e, n_h and $T_\mathrm{h} = 93\,\mathrm{keV}$ =constant for the so-called "off-axis" EP density profile here labelled "h". The equilibrium is reconstructed with the latest version of CHEASE (Lütjens et al. 1996) allowing the specification of q.

During the simulation, the energetic particle density profile changes rapidly in the beginning of the simulation. With XTOR-K, it relaxes towards the same shape as e.g. ORB5, but in a much shorter time, i.e. about 0.05 ms. With XTOR-K this behavior is characteristic of initial conditions that depart from a kinetic equilibrium. Indeed the Maxwellian particle distribution is initialized randomly in the torus using a static ideal MHD equilibrium configuration (Lütjens et al. 1996). Thus the particle distribution rearranges itself in order to reach a stationary equilibrium ($n = 0$) state (see Fig. 13, bottom row, right frame). The total energy evolution obtained with XTOR-K is very noisy because of the full-f PIC method. However, the time evolution of selected Fourier modes of a field can be extracted from the simulation at chosen radii. In Fig. 11 the timelines of the $m/n = 2/1$ and $m/n = 3/1$ components of the radial velocity field v^r are presented for $s = 0.199$ and $s = 0.451$. These two radii are in the proximity of dominant resonant surfaces of the two Alfvén modes of the present study.

The modes structures of $\sqrt{g_{ss}}v^r$ are given at $t = 0.248$ ms and $t = 0.605$ ms (see Fig. 12). The figures show the complex modulus of this quantity for poloidal mode numbers $m = 0, \ldots, 6$. At $t = 0.248$ ms the mode structure is dominated by the $m = 2$ component, and located around $s = 0.2$. At the end of the simulation a $n = 1$ TAE appears with dominant $m = 2, 3$ components radially located around $s = 0.4$. As already observed with the other codes, this TAE is rotating in opposite direction compared to the initial mode.

In the top Fig. 11, the evolution of the $m/n = 2/1$ and 3/1 components of v^r of the EPM are observed at $s = 0.2$. The $m/n = 2/1$ perturbation of the radial velocity due to this instability remains through the entire non-linear phase after its linear growth ending at $t = 0.25ms$. The amplitude of $m/n = 3/1$ component of this modes remains small. Simultaneously, bottom Fig. 11, a $m/n = 2/1$ and 3/1 TAE is growing at $s = 0.4$. The timeline at $s = 0.45$ shows the characteristic beating between the dominant $m = 2$ and 3 components of the modes, which reach comparable amplitudes. One remarks that $m = 2/1$ component of this

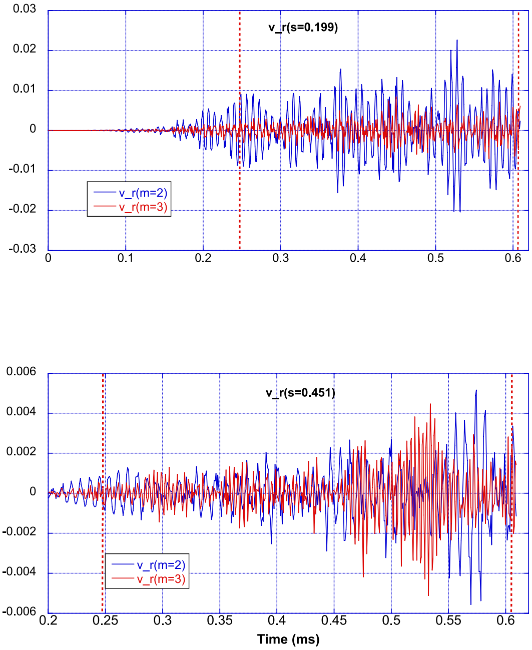

Fig. 11 Timelines of the $m/n = 2/1$ and $m/n = 3/1$ components of the radial velocity field v^r at radius $s = 0.199$ and $s = 0.451$. v^r is plotted in XTOR normalization. The two dotted red vertical lines correspond to the times in Fig. 12

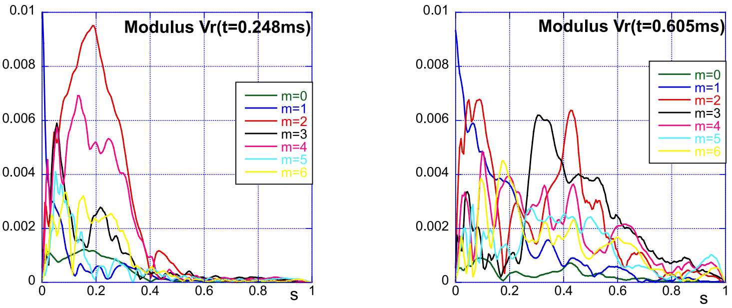

Fig. 12 Radial velocity component for the XTOR-K simulation, for early (left) and late (right) saturated phases

mode has two superposed frequencies, one corresponding to the inner EPM and the other one to the TAE. The TAE frequency appears in a very clean way on the $m = 3/1$ component.

The growth rates of both the EPM and the TAE are difficult to measure in the present case because the initial phase is merged in the numerical noise of the PIC method. However, the frequencies can be obtained from Fig. 11, giving $\omega = 166\,\mathrm{kHz}$ for the close-to-the-axis mode observed in the early phase of saturation, and $\omega = -196\,\mathrm{kHz}$ for the one observed in the late-saturated phase, in good agreement with what was observed by HYMAGYC, MEGA and ORB5.

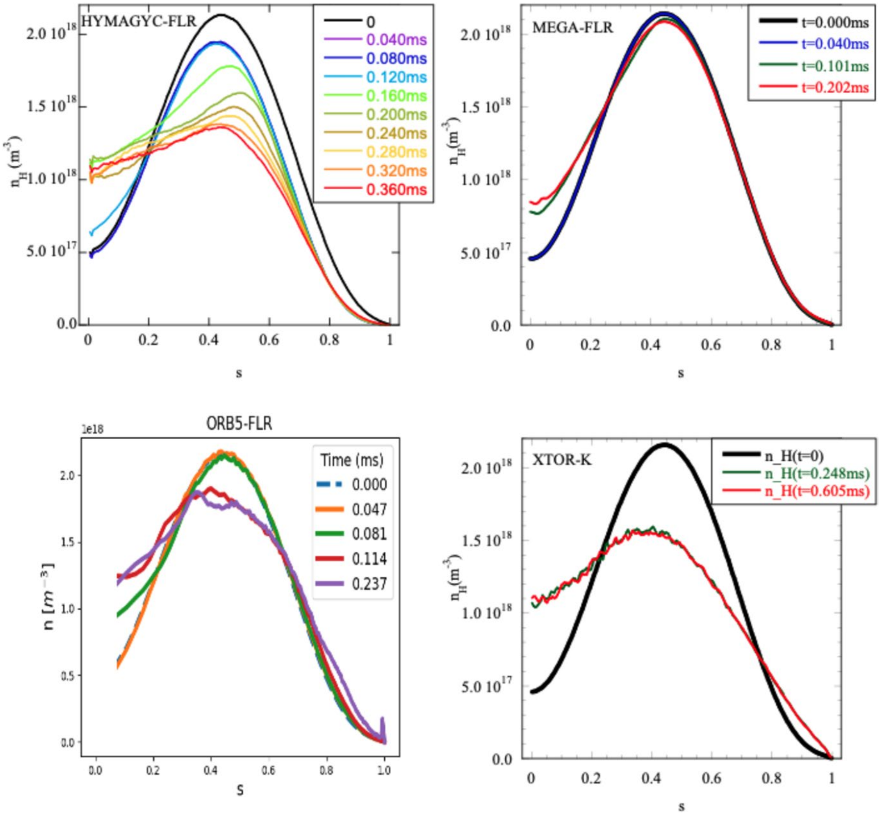

Fig. 13 Energetic particle density evolution as obtained by HYMAGYC (top row, left frame), MEGA (top row, right frame), ORB5 (bottom row, left frame) and XTOR-K (bottom row, right frame) non-linear simulations (note that the color code differs among different plots)

7 Conclusions

The result of a non-linear benchmark among few of the state-of-the-art codes available to study the self-consistent interaction of an EP population with shear Alfvén waves has been shown. The codes considered are HYMAGYC, MEGA, ORB5, and XTOR-K. The so-called NLED-AUG reference case with peaked off-axis EP density profile case, and using its shaped cross section version, has been considered. Qualitative agreement has been obtained, despite the different physical models considered (hybrid MHD-gyrokinetic, global electromagnetic gyrokinetic, MHD-kinetic). Note that in this non-linear benchmark, the results presented only refer to a single case, i.e., the nominal case, thus without any scanning in parameters space: we are aware that this choice would result in limiting the completeness of such a benchmark and we reserve for future work, the completion of such an exercise. These results are consistent with the state of the art theoretical understanding discussed in Chen and Zonca (2016). The case of a single toroidal mode number, $|n| = 1$, has been considered.

The result of the non-linear saturation of a linearly unstable EPM mode located close to the magnetic axis is the broadening of the EP density profile, which, for all four codes, is partially filled in close to the magnetic axis (see Fig. 13, which has already been briefly commented in the previous sections). Nevertheless, it has to be noted that the amount of transport toward the axis differs notably among the four codes: in particular, MEGA looks to have much lower transport than the other three codes.

This EPM is driven unstable by the internal part of the off-axis peaked energetic particle density profile, characterized by a positive EP radial density profile. It has to be noted that evidence of inward EP transport (Lauber 2020) has been, indeed, observed in AUG discharges with off-axis peaked EP density profile, although this evidence should not be considered as a validation between the results of this benchmark and the experiment, because of the various differences among the simulation setup and the AUG experimental shot. Later on, in the saturated phase, all the codes observe a second, subdominant, TAE mode, located in the external region of the plasma discharge, which rotates, in the poloidal plane, in the opposite direction of the first, dominant EPM mode. This second mode is excited by the external part of the EP density profile, characterized by a negative EP radial density profile, and could be responsible for further broadening of the EP radial density profile toward the edge. The dynamics of the appearance and evolution of this second, subdominant mode, while qualitatively similar, unveils various differences among the four codes, as, e.g., the time lapsed among the saturation of the dominant, linearly most unstable EPM, and the occurrence of the weaker, external TAE, and the associated EP transport toward the edge, which is quite strongly evident on ORB5 and XTOR-K, whereas in HYMAGYC and MEGA is only barely observable.

Some minor differences are observed when comparing simulations that retain only FOW and those that retain also FLR effects: typically, retaining FLR effects results in smaller growth rates and smaller saturation amplitudes.

Considering the effects on the EP transport induced by the EP-driven modes, in Fig. 14 two similar simulations, one with only FOW effects, and the other retaining also FLR effects, are compared for each of the three codes HYMAGYC, MEGA and ORB5. The simulations retaining only FOW effects result in higher EP transport, both toward the magnetic axis (thus filling more the internal hole in the profile) and toward the edge (see, e.g., the red curve (FOW) for $s \gtrsim 0.8$ in the first frame from the left, Fig. 14, in comparison to the blue curve (FLR), which corresponds to HYMAGYC simulations). Similar behavior is barely observed in MEGA simulations (second frame from the left) and, in a more pronounced figure, in ORB5 simulations (third frame from the left), where an evident "knee" is clearly observed (see, for $s \gtrsim 0.8$, the green curve (FOW) w.r.t. the orange curve (FLR)).

It is worth mentioning that one source of discrepancy between the results observed during the non-linear phase by MEGA on the one hand, and by HYMAGYC and XTOR-K on the other, could depend on the different scheme used to couple the EP species with the fluid one, i.e., the so-called "current coupling" used by MEGA, and the "pressure coupling" used by HYMAGYC and XTOR-K, as already mentioned

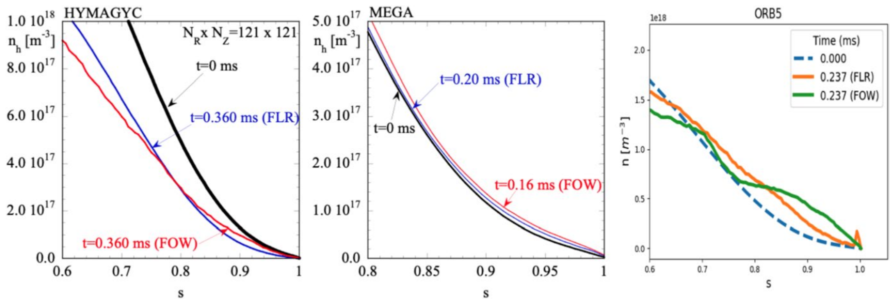

Fig. 14 Energetic particle density profiles in the long saturated phase: comparing simulations retaining only FOW or also FLR-HYMAGYC (energetic particle pressure computed using (R, Z) coordinates for both simulations, assuming $N_R \times N_Z = 121 \times 121$) (first frame from the left); MEGA (second frame from the left); ORB5 (third frame from the left). Note the different scales used for the ordinates and abscissas in the three figures to better distinguish the displayed curves

above. An other possible source of discrepancy among the codes considered in this benchmark may arise from the inclusion or not of the inertia of fast ions within the different models considered (hybrid codes vs. fully gyrokinetic ones), in particular for the equilibrium here considered, characterized by a high fraction of EPs w.r.t. the electron density: a quantification of this effect has not been done and will deserve future attention. An exhaustive and quantitative comparison between codes, that we devote for a near future work, will also have to adequately compare the obtained results as, e.g., the saturation level obtained by the different codes for the observed modes (the EPM near the magnetic axis and, subsequently, the outermost TAE), quantify the related radial transport of the EPs, describing and comparing the dynamics of EPs in full phase space. For such quantitative comparisons, the compliance of all the codes with a common database system (as, e.g., IMAS) would be a most important request. One may also use the self-consistent theoretical framework in Falessi (2023), Zonca (2015), Falessi and Zonca (2019) to validate the results and determine which of the simulations is closest to the theoretical predictions. In addition, the discrepancies uncovered in this work motivate a validation study, where the simulations are compared with the experimental evidence of AUG.

The non-linear benchmark presented in this review well fits into the overall picture of the simulation and modeling of transport and dynamics of energetic particles in ignited plasmas (Mishchenko 2023), as outlined at the beginning of Sect. 1. Indeed, this is a crucial point to be addressed in the next thermonuclear fusion devices. In particular, this benchmark contributes at verifying and validating effective tools for the construction of energetic particle transport models resolved in phase space, such as the one highlighted in Refs. Falessi (2023) and Lauber (2024). Validated, first principle based tools are required to better understand the mechanisms behind experimentally observed phenomena, and can serve as a reference for the construction and benchmarking of faster-execution and lower-fidelity level modules, necessary to move towards “flight-simulator” type instruments suited to more easily predict and design ignited plasma discharges. In summary, this brief review demonstrates that developing a reliable predicting capability of reactor-relevant burning plasmas is indeed possible and feasible, based on gyrokinetic and hybrid MHD-kinetic code simulations in support of a hierarchy of reduced models with different levels of approximation, which can be rigorously verified within one-single unified theoretical framework.

Equations of motion in HYMAGYC

Gyrocenter coordinates $(\mathbf{R}, M, U)$ are evolved in HYMAGYC according to the following equations (Brizard 1990):

$$\begin{aligned}\frac{dR^i}{dt} =& -\frac{e_h}{\Omega_h m_h}\epsilon^{ijk} b_k \left(1 - \frac{U}{\Omega_h}\epsilon^{lmn} b_l \partial_m b_n\right)\partial_j \Phi - \frac{M}{m_h}\epsilon^{ijk} b_k \partial_j \ln B + \\ & \left(b^i + \frac{U}{\Omega_h}\epsilon^{ijk} b_j b^l \partial_l b_k\right)\left(U + \frac{e_h}{m_h}\partial_U \Phi\right),\end{aligned} \tag{A1}$$

$$\frac{dM}{dt} = 0, \tag{A2}$$

$$\frac{dU}{dt} = -\frac{e_h}{m_h}\left(b^i + \frac{U}{\Omega_h}\epsilon^{ijk} b_j b^l \partial_l b_k\right)\partial_i \Phi - \frac{M\Omega_h}{m_h} b^i \partial_i \ln B, \tag{A3}$$

with

$$\Phi = < \overline{\delta\phi} > - \frac{U}{c} < b^i \overline{\delta A_i} > - \frac{\Omega_h}{c}\left(\frac{2M}{m_h \Omega_h}\right)^{1/2} < c^i(\vartheta)\overline{\delta A_i} > + O(\epsilon^2). \tag{A4}$$

Here, the last term represents all the higher-order terms in the gyrokinetic smallness parameter ϵ. The pedix h refers to energetic (hot) particles; $\mathbf{b}$ is the unit vector of the direction of the parallel magnetic field; $\mathbf{c}$ is the unit vector tangent to the Larmor orbit in the plane perpendicular to the equilibrium magnetic field. The quantity ϵ^{ijk} is the Levi-Civita symbol, and the Einstein notation for the summation over repeated indices has been adopted. The bars over the fluctuating scalar $(\delta\phi)$ and vector $(\delta\mathbf{A})$ potentials mean that they are computed at the particle position $\mathbf{R} + (2M/m_H\Omega_h)^{1/2}\mathbf{a}(\vartheta)$, with $\mathbf{a}$ being the unit vector pointing from the gyrocenter to the particle position. The average symbols $< \cdots >$ represent average over the gyrophase ϑ. These averages, as well as those required to compute the energetic-particle pressure tensor, are evaluated by a summation over N values of ϑ ($N = 32$, in the simulation presented in the present paper). In the cases in which only finite-orbit-width effects are retained, the average of each quantity is replaced by the value of that quantity in the gyrocenter $\mathbf{R}$. This corresponds to adopting a drift-kinetic approximation.

Acknowledgements The authors are grateful to Dr. H. Jhang for fruitful discussions. This work has been carried out within the framework of the EUROfusion Consortium, funded by the European Union via the Euratom Research and Training Programme (Grant Agreement No 101052200—EUROfusion), within the framework of the Enabling Research project ATEP and the EUROfusion Theory Simulation Verification and Validation task TSVV10. The Swiss contribution to this work has been funded by the Swiss State Secretariat for Education, Research and Innovation (SERI). Views and opinions expressed are, however, those of the author(s) only and do not necessarily reflect those of the European Union, the European Commission or SERI. Neither the European Union nor the European Commission nor SERI can be held responsible for them. Work partly supported by the Swiss National Science Foundation. Computations were performed mainly on the HPC-Marconi supercomputer, on the Piz Daint at CSCS, projects c14 and s1067, and on HPC resources from GENCI, France (Grant 2023-A0130500198). This work was supported in part by the Italian Ministry of Foreign Affairs and International Cooperation, grant number CN23GR02 and by the MMNLP project CSN4 of INFN, Italy.

Data availability The data that support the findings of this study are available from the corresponding author and/or the co-authors upon reasonable request.

Declarations

Conflict of interest Fulvio Zonca is an editorial board member for Reviews of Modern Plasma Physics and was not involved in the editorial review or the decision to publish this article. We confirm that there are no other known Conflict of interest associated with this publication and there has been no significant financial support for this work that could have influenced its outcome.

References

H. Abu-Shawareb et al., Phys. Rev. Lett. **132**, 065102 (2024). https://doi.org/10.1103/PhysRevLett.132.065102

A. Biancalani et al., Plasma Phys. Control. Fusion **63**, 065009 (2021). https://doi.org/10.1088/1361-6587/abf256

A. Bierwage, K. Shinohara, Y. Kazakov et al., Nat. Commun. **13**, 3941 (2022). https://doi.org/10.1038/s41467-022-31589-6

T.J. Bogaarts et al., Phys. Plasmas **29**, 122501 (2022). https://doi.org/10.1063/5.0119435

A. Bondeson, G. Vlad, H. Lütjens, IAEA Technical Committee Meeting on Advances in Simulations and Modelling of Thermonuclear Plasmas (15–18 June 1992) (Montreal (Canada)) (Vienna, Austria: International Atomic Energy Agency), p. 306 (1992)

A. Bondeson, G.Y. Fu, Comput. Phys. Commun. **66**, 167–76 (1991). https://doi.org/10.1016/0010-4655(91)90065-S

S. Briguglio, G. Vlad, F. Zonca, C. Kar, Phys. Plasmas **2**, 3711–23 (1995). https://doi.org/10.1063/1.871071

S. Briguglio, F. Zonca, G. Vlad, Phys. Plasmas **5**, 3287–301 (1998). https://doi.org/10.1063/1.872997

A. Brizard, Nonlinear gyrokinetic tokamak physics. Ph.D. thesis, Princeton University (1990). https://www.osti.gov/biblio/5019035

G. Brochard et al., Nucl. Fusion **60**, 086002 (2020). https://doi.org/10.1088/1741-4326/abb14b

G. Brochard et al., Nucl. Fusion **65**, 016052 (2025). https://doi.org/10.1088/1741-4326/ad8013

L. Chen, F. Zonca, Rev. Mod. Phys. **88**, 015008 (2016). https://doi.org/10.1103/RevModPhys.88.015008

J. Citrin, P. Mantica, Plasma Phys. Control. Fusion **65**, 033001 (2023). https://doi.org/10.1088/1361-6587/acab2b

G. Conroy, Nature **632**, 968 (2024). https://doi.org/10.1038/d41586-024-02759-x

A. Di Siena et al., Nucl. Fusion **63**, 106012 (2023). https://doi.org/10.1088/1741-4326/acf1b0

A. Di Siena, R. Bilato, T. Görler, E. Poli, A. Bañón Navarro, D. Jarema, F. Jenko, Plasma Phys. Control. Fusion **64**, 064003 (2022). https://doi.org/10.1088/1361-6587/ac6276

T. Donné, European Research Roadmap to the Realisation of Fusion Energy (2018). www.euro-fusion.org/eurofusion/roadmap (https://euro-fusion.org/wp-content/uploads/2022/10/2018_Research_roadmap_long_version_01.pdf)

S. Duan, X. Wang, H. Cai, D. Li, Nucl. Fusion **63**, 046002 (2023). https://doi.org/10.1088/1741-4326/acb802

M.V. Falessi et al., New J. Phys. **25**, 123035 (2023). https://doi.org/10.1088/1367-2630/ad127d

M.V. Falessi, F. Zonca, Phys. Plasmas **26**, 022305 (2019). https://doi.org/10.1063/1.5063874

M.V. Falessi, N. Carlevaro, V. Fusco, G. Vlad, F. Zonca, Phys. Plasmas **26**, 082502 (2019). https://doi.org/10.1063/1.5098982

M.V. Falessi, N. Carlevaro, V. Fusco, E. Giovannozzi, P. Lauber, G. Vlad, F. Zonca, J. Plasma Phys. **86**, 845860501 (2020). https://doi.org/10.1017/S0022377820000975

A. Fasoli, C. Gormenzano, H.L. Berk, B. Breizman, S. Briguglio, D.S. Darrow, N. Gorelenkov, W.W. Heidbrink, A. Jaun, S.V. Konovalov, R. Nazikian, J.-M. Noterdaeme, S. Sharapov, K. Shinohara, D. Testa, K. Tobita, Y. Todo, G. Vlad, F. Zonca, Chapter 5: Physics of Energetic Ions. Nucl. Fusion **47**, 264 (2007). https://doi.org/10.1088/0029-5515/47/6/S05

G. Federici et al., Fusion Eng. Des. **136**, 729–741 (2018). https://doi.org/10.1016/j.fusengdes.2018.04.001

G. Fogaccia, G. Vlad, S. Briguglio, Nucl. Fusion **56**, 112004 (2016). https://doi.org/10.1088/0029-5515/56/11/112004

G.Y. Fu, W. Park, H.R. Strauss, J. Breslau, J. Chen, S. Jardin, L.E. Sugiyama, Phys. Plasmas **13**, 052517 (2006). https://doi.org/10.1063/1.2203604

R.C. Grimm, R.L. Dewar, J. Manickam, J. Comput. Phys. **49**, 94 (1983). https://doi.org/10.1016/0021-9991(83)90116-X

T.S. Hahm et al., Phys. Plasmas **30**, 072501 (2023). https://doi.org/10.1063/5.0151466

H. Han et al., Nature **609**, 269 (2022). https://doi.org/10.1038/s41586-022-05008-1

J. Hobirk et al., Nucl. Fusion **63**, 112001 (2023). https://doi.org/10.1088/1741-4326/acde8d

S.H. Hong, A Review of DEMO Reactor Concepts: Open Questions and Issues. AAPPS Bull. **32**, 10 (2022). https://doi.org/10.1007/s43673-022-00040-9

A. Ishizawa, K. Imadera, Y. Nakamura, Y. Kishimoto, Nucl. Fusion **61**, 114002 (2021). https://doi.org/10.1088/1741-4326/ac1f61

ITER Physics Expert Group on Energetic Particles, Heating and Current Drive and ITER Physics Basis Editors *Chapter 5: Physics of energetic ions*, Nucl. Fusion **39**, 2471 (1999). https://doi.org/10.1088/0029-5515/39/12/305

ITER Web page: https://www.iter.org/

F. Jenko, W. Dorland, M. Kotschenreuther, B.N. Rogers, Phys. Plasmas **7**, 1904–10 (2000). https://doi.org/10.1063/1.874014

H. Jhang et al., Plasma Phys. Control. Fusion **65**, 095018 (2023). https://doi.org/10.1088/1361-6587/ace3f2

S. Jolliet et al., Comput. Phys. Commun. **177**, 409–425 (2007). https://doi.org/10.1016/j.cpc.2007.04.006

JT-60SA Web page: https://www.jt60sa.org/wp/

D. Kim et al., Nucl. Fusion **63**, 124001 (2023). https://doi.org/10.1088/1741-4326/acffda

E. Lanti et al., Comput. Phys. Commun. **251**, 107072 (2020). https://doi.org/10.1016/j.cpc.2019.107072

Ph. Lauber et al., Nucl. Fusion **64**, 096010 (2024). https://doi.org/10.1088/1741-4326/ad6336

X. Litaudon et al., Plasma Phys. Control. Fusion **64**, 034005 (2022). https://doi.org/10.1088/1361-6587/ac44e4

P. Liu, X. Wei, Z. Lin, G. Brochard, G.J. Choi, W.W. Heidbrink, J.H. Nicolau, G.R. McKee, Phys. Rev. Lett. **128**, 185001 (2022). https://doi.org/10.1103/PhysRevLett.128.185001

H. Lütjens, A. Bondeson, O. Sauter, Comput. Phys. Commun. **97**, 219–60 (1996). https://doi.org/10.1016/0010-4655(96)00046-X

R. Martone, R. Albanese, F. Crisanti, P. Martin, A. Pizzuto (eds.) DTT Divertor Tokamak Test facility—Interim Design Report (2019). ISBN 978-88-8286-378-4. https://www.dtt-project.it/DTT_IDR_2019_WEB.pdf

MET Enabling Research Project 2019–2020. https://afs.enea.it/zonca/METproject/index.html

A. Mishchenko et al., Comput. Phys. Commun. **238**, 194–202 (2019). https://doi.org/10.1016/j.cpc.2018.12.002

A. Mishchenko et al., Plasma Phys. Control. Fusion **65**, 064001 (2023). https://doi.org/10.1088/1361-6587/acce68

W. Park et al., Phys. Fluids B **4**, 2033 (1992). https://doi.org/10.1063/1.860011

Ph. Lauber et al., "Energetic Particle dynamics induced by off-axis neutral beam injection on ASDEX Upgrade, JT-60SA and ITER" 28th IAEA FEC (2020), p. 1074. https://conferences.iaea.org/event/214/contributions/17169/

Ph. Lauber et al., Strongly Nonlinear Energetic Particle Dynamics in ASDEX-Upgrade Scenarios with Core Impurity Accumulation (22–27 October 2018 Ahmedabad, India), in *27th IAEA Fusion Energy Conference (Proc. 27th IAEA FEC (2018))*. https://conferences.iaea.org/event/151/contributions/6094/

Ph. Lauber, "The NLED reference case", ASDEX Upgrade Ringberg Seminar (Ph. Lauber et al, NLED-AUG reference case http://www2.ipp.mpg.de/~pwl/NLED_AUG/data.html) (2016)

S.D. Pinches, I.T. Chapman, P.W. Lauber, H. Oliver, S.E. Sharapov, K. Shinohara, K. Tani, Phys. Plasmas **22**, 021807 (2015). https://doi.org/10.1063/1.4908551

Z. Qiu, L. Chen, F. Zonca, Rev. Modern Plasma Phys. **7**, 28 (2023). https://doi.org/10.1007/s41614-023-00130-7

O. Sauter, S.Y. Medvedev, Comput. Phys. Commun. **184**, 293 (2013). https://doi.org/10.1016/j.cpc.2012.09.010

Special Issue of *Special Issue for the Engineering Design of Chinese Fusion Engineering Test Reactor (CFETR)* (2022). https://www.sciencedirect.com/special-issue/10S83P1177T

Y. Todo, Phys. Plasmas **13**, 082503 (2006). https://doi.org/10.1063/1.2234296

Y. Todo, Rev. Modern Plasma Phys. **3**, 1 (2019). https://doi.org/10.1007/s41614-018-0022-9

F. Vannini et al., Nucl. Fusion **62**, 126042 (2022). https://doi.org/10.1088/1741-4326/ac8b1e

G. Vlad et al., Non-linear benchmark between HYMAGYC, MEGA, ORB5 AND XTOR-K codes using the NLED-AUG test case to study Alfvénic modes driven by energetic particles, (16–21 October 2023 London, UK), in *29th IAEA Fusion Energy Conference (Proc. 29th IAEA FEC (2023))*. https://conferences.iaea.org/event/316/contributions/

G. Vlad et al., Nucl. Fusion **61**, 116026 (2021). https://doi.org/10.1088/1741-4326/ac2522

G. Vlad, F. Zonca, S. Briguglio, Rivista del Nuovo Cimento **22**(7), 1–97 (1999). https://doi.org/10.1007/BF02874568

G. Vlad, S. Briguglio, G. Fogaccia, B. Di Martino, Comput. Phys. Commun. **134**(1), 58–77 (2001). https://doi.org/10.1016/S0010-4655(00)00191-0

R.E. Waltz, E.M. Bass, Nucl. Fusion **54**, 104006 (2014). https://doi.org/10.1088/0029-5515/54/10/104006

X. Wang et al., Phys. Plasmas **29**, 032512 (2022). https://doi.org/10.1063/5.0080785

X. Wang et al., Plasma Phys. Control. Fusion **65**, 074001 (2023). https://doi.org/10.1088/1361-6587/acd71f

T. Wang, X. Wang, S. Briguglio, Z. Qiu, G. Vlad, F. Zonca, Phys. Plasmas **26**, 012504 (2019). https://doi.org/10.1063/1.5064863

T. Wang, Z. Qiu, F. Zonca, S. Briguglio, G. Vlad, Nucl. Fusion **60**, 126032 (2020). https://doi.org/10.1088/1741-4326/abb2d4

T. Wang, S. Wei, S. Briguglio, G. Vlad, F. Zonca, Z. Qiu, Plasma Sci. Technol **26**, 053001 (2024). https://doi.org/10.1088/2058-6272/ad15e0

H. Wang, P.W. Lauber, Y. Todo, Y. Suzuki, H. Li, J. Wang, S. Wei, Nucl. Fusion **64**, 076015 (2024). https://doi.org/10.1088/1741-4326/ad4a8d

L.L. Zhang et al., Nucl. Fusion **64**, 076001 (2024). https://doi.org/10.1088/1741-4326/ad4535

F. Zonca et al., New J. Phys. **17**, 013052 (2015). https://doi.org/10.1088/1367-2630/17/1/013052

Authors and Affiliations

Gregorio Vlad[1] · Xin Wang[2] · Francesco Vannini[2] · Hinrich Lütjens[3] · Sergio Briguglio[1] · Nakia Carlevaro[1] · Matteo V. Falessi[1,4] · Giuliana Fogaccia[1] · Valeria Fusco[1] · Fulvio Zonca[1,5] · Alessandro Biancalani[6] · Alberto Bottino[2] · Thomas Hayward-Schneider[2] · Philipp Lauber[2] · Baruch Rofman[7] · Laurent Villard[7]

✉ Gregorio Vlad
gregorio.vlad@enea.it

Xin Wang
xin.wang@ipp.mpg.de

Francesco Vannini
frn.vanni@gmail.com

Hinrich Lütjens
hinrich.lutjens@polytechnique.edu

Sergio Briguglio
sergio.briguglio@enea.it

Nakia Carlevaro
nakia.carlevaro@enea.it

Matteo V. Falessi
matteo.falessi@enea.it

Giuliana Fogaccia
giuliana.fogaccia@enea.it

Valeria Fusco
valeria.fusco@enea.it

Fulvio Zonca
fulvio.zonca@enea.it

Alessandro Biancalani
alessandro.biancalani@devinci.fr

Alberto Bottino
bottino@ipp.mpg.de

Thomas Hayward-Schneider
thomas.hayward@ipp.mpg.de

Philipp Lauber
pwl@ipp.mpg.de

Baruch Rofman
baruch.rofman@epfl.ch

Laurent Villard
laurent.villard@epfl.ch

[1] ENEA, Nuclear Department, C. R. Frascati, Via E. Fermi 45, 00044 Frascati, Rome, Italy

[2] Max-Planck-Institut für Plasmaphysik, Boltzmannstr. 2, 85748 Garching, Germany

[3] CNRS, École Polytechnique, Institut Polytechnique de Paris, Palaiseau, France

[4] Istituto Nazionale di Fisica Nucleare (INFN), Sezione di Roma, P.le Aldo Moro 2, 00185 Rome, Italy

[5] Institute for Fusion Theory and Simulation, Department of Physics, Zhejiang University, Hangzhou 310027, People's Republic of China

[6] De Vinci Higher Education, De Vinci Research Center, 92916 Paris, France

[7] Swiss Plasma Center, EPFL, Lausanne, Switzerland